CrossMark

Reaction pathway for synthesis of Cu₂ZnSn(S/Se)₄ via mechano-chemical route and annealing studies

Devendra Pareek[1] · K. R. Balasubramaniam[1] · Pratibha Sharma[1]

Abstract Reaction pathway for the formation of kesterite $Cu_2ZnSn(S/Se)_4$ (CZTS/Se) from elemental precursors (Cu, Zn, Sn, S/Se) has been investigated experimentally and is being reported in the current paper. To identify the various stages of reaction pathway and to identify the formation and consumption of secondary phases, X-ray diffraction and Raman spectroscopy tools were employed. A series of experiments for different ballmilling durations (5, 10, 15, 20, 25 and 30 h) were performed and the presence of different phases was recorded for each experiment. In addition to XRD and Raman studies, phase formation has also been confirmed using detailed XPS, TEM and SEM–EDS analysis. In addition, the effect of annealing temperature on composition and band gap of the CZTS/Se material has been discussed. Optical band gap of various samples of CZTS was observed in the range of 1.40–1.60 eV and that of CZTSe was observed in the range of 1.08–1.18 eV. The relatively simple, low cost, easily scalable mechanical alloying process along with understanding of reaction pathway will provide a future scope for bulk production of CZTS/Se absorber material for thin film solar cells.

1 Introduction

The increasing perception of CZTS/Se materials as a potential absorber material for next generation solar photovoltaic is reflected in the large variety of routes that have been undertaken for thin-film deposition. These include the various vacuum based approach such as sputtering [1–7], evaporation [8–20], pulsed laser deposition [21–26] and non-vacuum based synthesis techniques such as Electro deposition [27–35], solution based approaches [36–49] and other techniques such as ballmilling [42, 43, 50–53] etc. As of now the best achieved efficiencies are 8.4 % [20] and 9.7 % [54] for CZTS and CZTSe respectively. In five consecutive years from 2010 to 2014, IBM has reported record efficiency of 9.6, 10.1, 11.1 and 12.6 % using CZTSSe material by hydrazine processing [55–58]. Still, the record efficiency of CZTSSe is far away from the best silicon, CIGS, and CdTe solar cells, that have efficiencies of 25.6, 21.7 and 21.5 % respectively [59]. Even if we consider the process corresponding to highest reported efficiency i.e. the Hydrazine based solution technique, the use of hazardous materials makes its acceptability difficult for bulk production. The other techniques such as sputtering, evaporation, PLD etc. are promising but looking at the current global interest on low cost material as well as processing technique, the most promising option left is environmental friendly solution based techniques. For each of these synthesis approaches, one major barrier is very limited understanding of CZTS as well as CZTSe phase diagram and control on the required phases during material synthesis [16, 60, 61], which makes it difficult to achieve single phase material. Another major difficulty is in achieving control in the material composition during processing steps like heating, due to volatility of materials such as Sn, Zn and S [62]. The above mentioned issues can

✉ Devendra Pareek
devpareek@iitb.ac.in

1 Department of Energy Science and Engineering, Indian Institute of Technology Bombay, Powai, Mumbai 400076, India

be resolved by developing a deep understanding of the formation of secondary phases and achieving control on them. The desired phase purity of CZTS/Se which is one of the key requirement in obtaining the better device performance can be achieved by understanding the reaction pathway during the material synthesis. Literature reports reveals that even the commercially well developed and easily scalable techniques such as ballmilling is also a promising route for obtaining near phase pure material [42, 50, 63]. Due to induction of the reaction by mechanical energy (momentum exchange by impact of balls), the reactive ballmilling process can introduce structural changes and can facilitate chemical reactions that in general occur at medium to high temperature to take place at near room temperature [64]. This makes the ballmilling process more suitable option for exothermic reactions [50]. Materials such as complex alkali metal hydrides [65], battery materials like $LiFePO_4$ [66] and solar PV materials like CZTS [43, 50–53, 67], CIGS [64], CdTe [68], $Cu_2ZnSnTe_4$ [69] and $CuInSe_2$ [70], have been synthesized via reactive ballmilling. In the current paper, experimentally observed reaction pathways during synthesis of CZTS as well as CZTSe via ball milling are being reported, which are so far not reported by mechano-chemical process. A series of ballmilling experiments using optimized experimental parameters [50], were performed. The phases formed during the various stages in the experiments of different durations were examined using XRD and Raman spectroscopy. The effect of annealing on both the stoichiometry and the band gap of CZTS/Se was also studied in the temperature range of 300–700 °C. In addition to XRD and Raman analysis a detailed TEM, XPS and SEM–EDS analysis of the samples are being presented.

2 Experimental details

2.1 Raw materials

Elemental powders of Cu (5.0837 g), Zn (2.6152 g), Sn (4.7484 g) and S (5.1304 g) (Sigma-Aldrich) with purity >99.5 % were fed into the ballmill bowl of 80 ml capacity for preparation of CZTS (Cu_2ZnSnS_4). Similarly, for preparation of the CZTSe ($Cu_2ZnSnSe_4$) compound, elemental powders of Cu (3.5586 g), Zn (1.8306 g), Sn (3.3239 g) and Se (8.8435 g) (Sigma-Aldrich) with purity >99.5 % were used. 1-butanol was added as a wet medium during ballmilling.

2.2 Synthesis procedure

Materials were synthesized by the procedure as reported in our earlier publication [50]. In short, the metal elements

(Cu, Zn, Sn) and chalcogenide powders were ballmilled at a speed of 450 RPM. A series of experiments for different milling duration were carried out separately, to understand the reaction pathway during synthesis of CZTS/Se. After completion of the experiment, the initial grey colored mixture transformed to a dark black colloidal solution. Thin films of the CZTS as well as CZTSe samples dispersed in1-butanol were deposited onto glass substrate using spin coater and dried at 60 °C on a hot plate. These films were then subjected to various annealing treatments in N_2 atmosphere at temperature ranging from 300 to 700 °C for 5 min. A heating rate of ~10 °C/min was used and the samples were allowed to cool down to room temperature, before removal from the furnace.

2.3 Material characterization

Thin films of as-synthesized and annealed sample of CZTS/Se were characterized by X-ray diffraction patterns using Panalytical X'Pert-Pro (Cu K-α radiation, 1.5418 Å) diffractometer. Jobvin–Yvon–Horiba (HR800UV) Raman spectrometer at ambient conditions equipped with a laser (514.5 nm) was used to obtain the Laser Raman Spectrum. TEM diffraction patterns were obtained on a Philips CM 200, operating at 20–200 kV accelerating voltage and having a resolution of ~2.4 Å. Field Emission Gun-Scanning Electron Microscope (FEG-SEM), JSM-7600F model, operating at an accelerating voltage of 0.1–30 kV, magnification range of 25–1,000,000× and having resolution 1.0–1.5 nm (15 kV) was used for energy dispersive X-ray spectroscopy (EDS) analysis. Thickness of the films were measured using Zeta Instruments make non-contact, optical profiler (Model: Zeta-20). Perkin-Elmer Lambda-950 spectrometer was used for optical characterization of the thin films of as synthesized as well as annealed samples.

3 Results and discussions

To understand the reaction pathway during CZTS and CZTSe formation from elemental precursors using ballmilling process, separate experiments were carried out for various milling durations (5, 10, 15, 20, 25 and 30 h). Figure 1a, b represents the XRD pattern of the various samples obtained from various ballmilling experiments of 5–30 h duration. It can be seen in Fig. 1a that in the sample corresponding to 5 h of ballmilling, peaks corresponding to binary phases such as Cu_2S (PDF card no: 01-072-1071), SnS_2 (PDF card no: 0121-1231) and ZnS (PDF card no: 01-089-2423) are appearing which indicates the occurrence of reaction among elemental precursors. Sample corresponding to 10 h of ballmilling shows the reduction in the
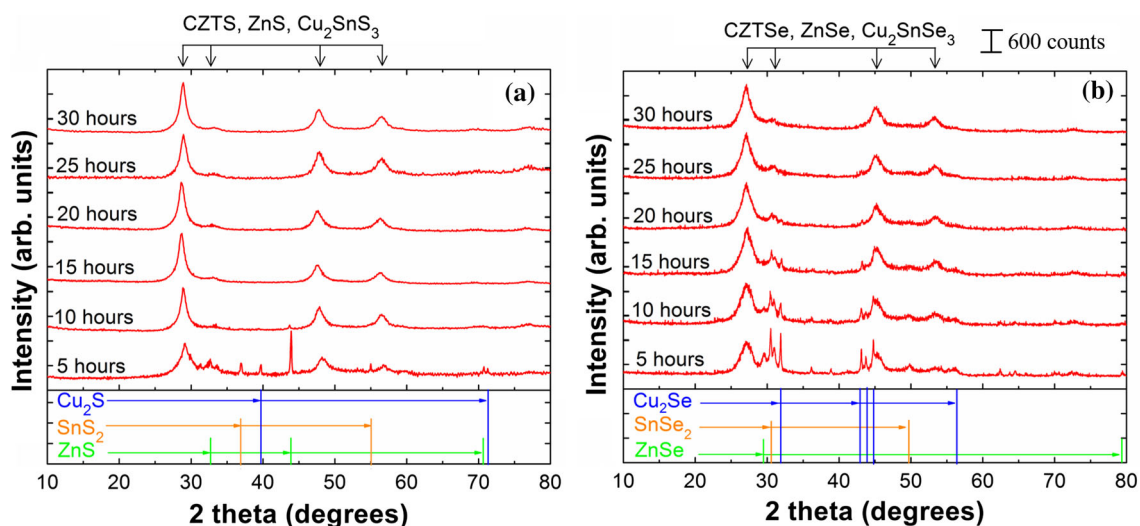
Fig. 1 XRD patterns of wet ballmilled precursors (Cu, Zn, Sn, Se and S) for synthesis of CZTS (**a**) and CZTSe (**b**) for various durations of milling. Peak positions related to CZTS/Se, ZnS/Se and $Cu_2Sn(S/Se)_3$ are shown by *arrows* at the *top* of XRD spectra (**a**, **b**)

intensity of binary phases. For the samples obtained after more than 10 h of ballmilling, all observed XRD peaks are in good agreement with literature reports on CZTS. However, these peaks could also be indexed to ZnS and Cu_2SnS_3, therefore further confirmation of phase was done using Raman spectra of these samples, Fig. 2a. Sample that has been prepared during 30 h ballmilling experiment exhibited major XRD peaks at $2\theta = 28.71°$ [d = 3.107 Å, (112) plane], 47.61° [d = 1.908 Å, (220) plane] and 56.35° [d = 1.631 Å, (312) plane].

The XRD patterns of the CZTSe samples synthesized during different ballmilling experiments of various durations are shown in Fig. 1b. Similar to CZTS, for CZTSe sample prepared by 5 h ballmilling experiment, peaks corresponding to binary phases such as Cu_2Se (PDF card nos: 01-088-2043 and 027-1131), $SnSe_2$ (023-0602) and ZnSe (01-080-0008) are present. In case of sample corresponding to 10 h duration experiment, the peaks of binary phases start diminishing. The peaks of binary phases are also appearing in the samples obtained after 15, 20 and 25 h duration experiments although the intensity is reducing with increasing ballmilling duration. The samples prepared after 30 h experiment shows peaks corresponding to either CZTSe or ZnSe and Cu_2SnSe_3 with no indication
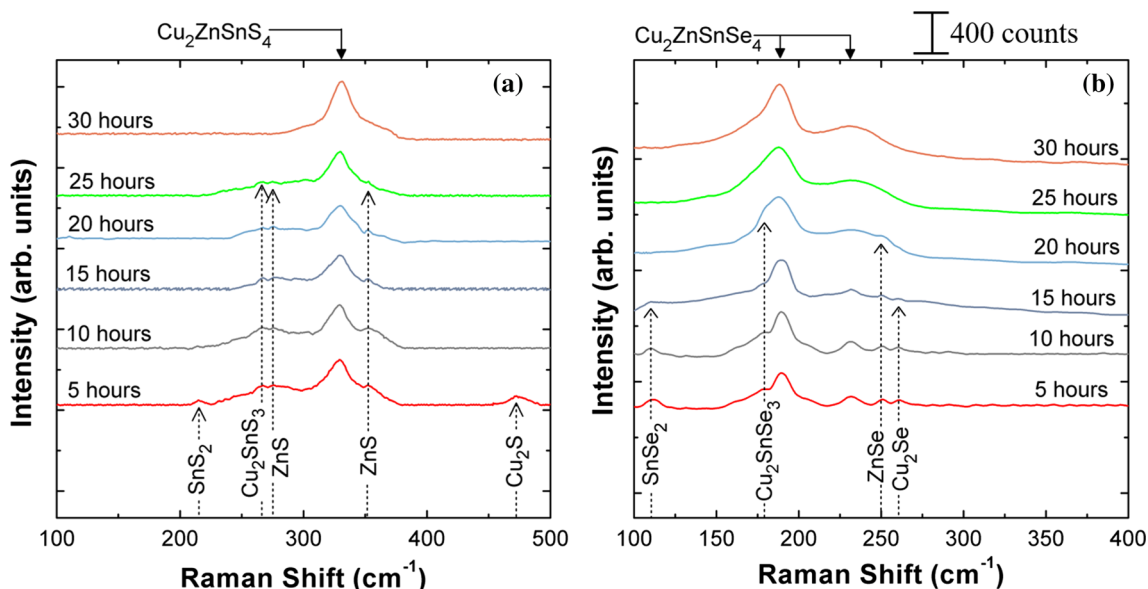
Fig. 2 Raman spectra of sample prepared during various durations of ballmilling experiments for CZTS (**a**) and CZTSe (**b**) synthesis. *Arrows* shown at the *top* of Raman spectra (**a**, **b**) represents the Raman peak position corresponding to CZTS and CZTSe

of presence of binary phases such as Cu_2Se and $SnSe_2$. Although similar to CZTS compound, the phase confirmation was done after analysis of Raman spectra (Fig. 2b), because of the existence of similar peaks positions for CZTSe, Cu_2SnSe_3 and ZnSe. The XRD patterns of CZTSe sample corresponding to 30 h duration milling experiment exhibited major peaks at $2\theta = 27.44°$ [d = 3.248 Å, (112) plane], 45.44° [d = 1.994 Å, (220) plane] and 53.67° [d = 1.706 Å, (312) plane].

The Raman spectra of the ballmilled elemental precursors as shown in Fig. 2a explain the reaction pathway of the CZTS formation. It can be clearly seen that for sample corresponding to 5 h milling duration the Raman peaks corresponding to quaternary phase CZTS (331 cm^{-1}), ternary phase Cu_2SnS_3 (267 cm^{-1}) and binary phases such as Cu_2S (472–474 cm^{-1}), ZnS (273–275, 350–353 cm^{-1}) and SnS_2 (215 cm^{-1}) can be seen, which is similar to the findings of XRD analysis as discussed in earlier part. Further the samples obtained on 10 h milling shows no clear indication of Cu_2S and SnS_2 phases. For the same sample, very low intensity peaks of binary phases were present in the XRD pattern. The reason for this could be the existence of very small amount of binary phases and the less penetration depth of laser source in Raman spectrometer might not have detected the same. Samples prepared with 15, 20 and 25 h of milling experiments show the peaks corresponding to CZTS, ZnS and Cu_2SnS_3, which is in good agreement to the XRD data of these samples (Fig. 1a). Further, it can be inferred that the intensities of the peaks other than CZTS are reducing by increasing the ballmilling duration. The sample prepared after 30 h of ballmilling shows the Raman peak corresponding to only CZTS with no evidence of any other secondary phase.

Figure 2b explains the reaction pathway of the CZTSe formation using elemental precursors. It can be clearly seen that in addition to quaternary phase; binary and ternary phases are also present in all the samples prepared with experiment duration ≤15 h. The same is also evident from XRD pattern as shown in Fig. 1b except presence of a less intense peak of Cu_2Se in sample prepared during 20 and 25 h of ballmilling. The same peak is not clearly visible in Raman spectrum, which might be due to presence of very less amount of Cu_2Se in the analyzed sample. Further the samples prepared after ballmilling operation for 30 h duration shows no indication of Cu_2Se (261–263 cm^{-1}), $SnSe_2$ (110 cm^{-1}), ZnSe (249–253 cm^{-1}) and Cu_2SnSe_3 (179–186 cm^{-1}) phases.

It can be deduced that in case CZTSe synthesis, binary phases such as Cu_2Se and $SnSe_2$ were present for longer duration (i.e. till 15 h) as compared to that in case of CZTS (i.e. Cu_2S and SnS_2 were present till <10 h experiments). The presence of binary selenide for longer duration is due to the fact that the reaction of formation of Cu_2SnSe_3 is less

exothermic as compared to that of Cu_2SnS_3 [H_f^o(Cu_2SnSe_3) = −2.116 eV/formula unit and H_f^o(Cu_2SnS_3) = −2.680 eV/formula unit [71]]. Considering the above discussion on XRD and Raman spectra of the various samples of ballmilled elemental powders, a reaction pathway for formation of quaternary phase Cu_2ZnSnX_4 (X: S, Se) can be determined, which is shown in the reaction sequence below:

$$2Cu + Zn + Sn + 4X \rightarrow Cu_2X + SnX_2 + ZnX$$
$$\rightarrow Cu_2SnX_3 + ZnX \rightarrow Cu_2ZnSnX_4$$
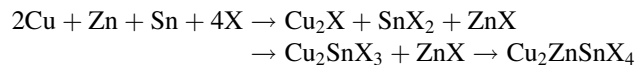
It is worth mentioning here that the reaction of binary sulphide/selenide to form quaternary Cu_2ZnSnX_4 is reversible, in which the forward reaction is less favourable at higher temperatures. The advantage of using ballmilling or any similar near room temperature process in promoting the reaction along forward direction is discussed elsewhere [50, 72].

To further confirm the phase purity of the CZTS as well as CZTSe samples prepared after 30 h of experiment, oxidation states of the elements were determined using high resolution (HR) XPS spectra. HR-XPS core level spectra, as shown in Fig. 3 confirms the presence of Cu^{+1}, Zn^{+2}, Sn^{+4}, S^{-2} ions in CZTS sample (Fig. 3a–d) and Cu^{+1}, Zn^{+2}, Sn^{+4}, Se^{-2} ions in CZTSe sample (Fig. 3e–h). The Cu 2p core level spectrum as shown in Fig. 3a exhibits binding energies (BE) peaks for the Cu 2p$_{3/2}$ (931.9 eV) and Cu 2p$_{1/2}$ (951.7 eV) with a peak splitting of 19.8 eV, confirms the Cu$^+$ oxidation state [73–75]. In case of Zn (Fig. 3b), BE values of 1022.3 and 1045.4 eV for Zn 2p$_{3/2}$ and Zn 2p$_{1/2}$ with peak splitting of 23.1 eV, suggesting the presence of only Zn^{2+} [42, 76]. The Sn 3d$_{5/2}$ and Sn 3d$_{3/2}$ peaks shown in Fig. 3c are present at 486.4 and 494.5 eV, respectively, with a separation of 8.1 eV, attributing to Sn (IV) [76, 77]. Figure 3d shows the S 2p core level spectrum which exhibit two peaks 2p3/2 and 2p1/2 with binding energy at 162.1 and 162.9 eV and a peak splitting of 0.8 eV, which are consistent with the 160–164 eV range expected for S in sulphide phases [74, 76].

Figure 3e shows the HR-XPS spectrum of CZTSe where two symmetric peaks at 931.9 and 951.6 eV with a peak splitting of 19.7 eV, represent the characteristic of Cu (I). In Fig. 3f zinc 2p peaks located at 1022.3 and 1045.2 eV show a peak separation of 22.9 eV, corresponding to Zn (II). The Sn 3d peaks located at 486.1 and 494.6 eV with a peak splitting of 8.5 eV, indicates Sn (IV) (Fig. 3g). The Se 3d doublet separation of 0.8 eV as shown in Fig. 3h, can be assigned to the formation of metal selenides (3d$_{3/2}$ at 54.2 eV and 3d$_{5/2}$ at 53.4 eV), which is consistent with the literature [78]. Since XPS peak corresponding to Cu^{+2} is absent in both the samples, therefore, the possibility of
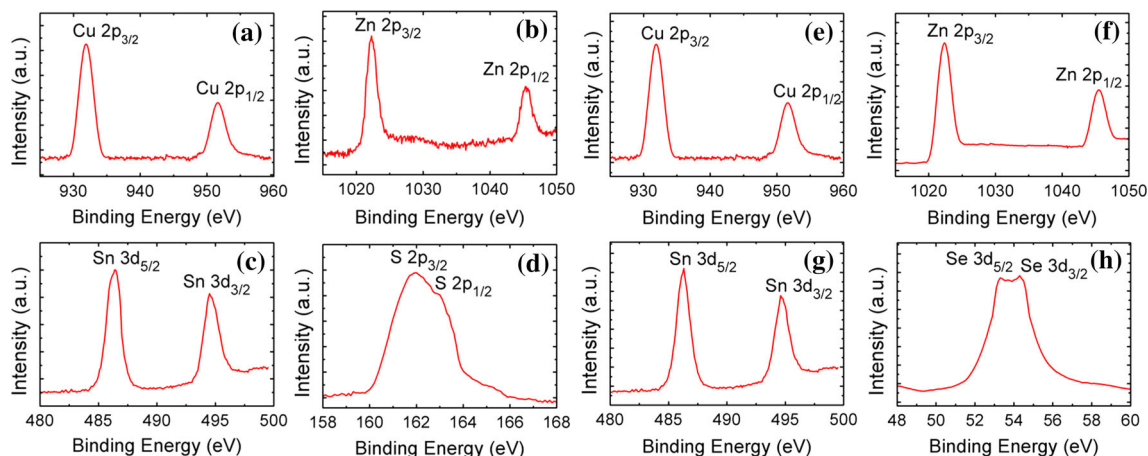
Fig. 3 High resolution XPS core level spectra of 30 h ballmilled elemental precursors used for synthesis of CZTS (**a–d**) and CZTSe (**e–h**)

formation of Cu_3SnS_4 and Cu_3SnSe_4 can be ruled out. Further, the absence of peaks corresponding to elemental constituent verifies the completion of reaction.

To further validate the quaternary phase formation, TEM studies were carried out for both the CZTS as well as CZTSe samples corresponding to 30 h of milling experiment. The results obtained from these studies are shown in Fig. 4. The HREM images for a CZTS particle shown in Fig. 4a exhibits lattice fringes corresponding to the (112) (d = 0.313 nm), (200) (d = 0.269 nm) lattice planes. HREM image of a CZTSe particle shown in Fig. 4c exhibits lattice fringes corresponding to the (112) (d = 0.327 nm) and (200) (d = 0.284 nm) planes of CZTSe, implying that this crystallite distribution is predominant, consistent with the results of Fig. 1. Similarly, various such particles were analyzed for both CZTS as well as CZTSe; most of them exhibited lattice fringes corresponding to (112), (220), (312), and (200) planes of CZTS and CZTSe.

The three most intense reflections for the kesterite structure are also present in the SAED patterns (Fig. 4b, d) that exhibited a ring pattern, consistent with the polycrystalline nature of the samples. The planes corresponding to each ring were assigned using diffraction ring profiler [79]. The simulated SAED ring pattern (left portion of Fig. 4b, d) was obtained using the standard CIF files of CZTS (ICSD code: 628891) and CZTSe (ICSD code: 189791). It can be clearly seen that the obtained ring pattern (right portion of Fig. 4c, d) matches perfectly with the simulated pattern.

After confirmation of the phase purity, CZTS sample corresponding to 30 h wet ball milling experiment was subjected to annealing at various temperatures (i.e. 300, 400, 500, 600 and 700 °C). Figure 5 shows the XRD patterns of as synthesized CZTS samples as well as the samples annealed at various temperatures.

As already mentioned earlier (Fig. 1a), the as-synthesized sample of CZTS shown in Fig. 5a exhibits major peaks at $2\theta = 28.71°$, 47.61° and 56.35°, corresponding to d-spacings of 3.107, 1.908 and 1.631 Å. XRD pattern corresponding to the CZTS sample, annealed at 300 °C (Fig. 5b), exhibits major peaks at 2θ values of 28.56°, 47.53° and 56.33° corresponding to d-spacings of 3.122, 1.911 and 1.631 Å respectively. The sample corresponding to annealing at 400 °C (Fig. 5c) exhibits major peaks at $2\theta = 28.51°$, 47.46° and 56.26° corresponding to d-spacings of 3.127, 1.913 and 1.633 Å respectively. Similarly, the sample corresponding to 500 °C annealing temperature (Fig. 5d) exhibits peaks at $2\theta = 28.49°$, 47.39° and 56.22° corresponding to d-spacings of 3.130, 1.917 and 1.635 Å.

In case of samples annealed at 600 °C (Fig. 5e), in addition to the peaks corresponding to CZTS, peaks of binary phases such as; Cu_2S (ICDD card no: 00-003-1071), CuS (ICDD card no: 01-078-2122) and SnS (ICDD card no: 00-022-0953) are also present.

This indicates that the higher temperature favours the occurrence of the backward movement in the following reaction:

$$Cu_2S + SnS_2 + ZnS \leftrightarrow Cu_2ZnSnS_4 \qquad (1)$$
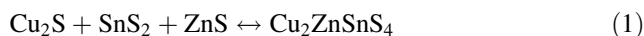
Thermodynamic arguments provided by Baryshev and Thimsen [72], supports our experimental findings, where by calculation of Gibb's free energy, it has been proved that, at T > 550 °C, the reverse reaction is more favorable in (1). Similarly, in case of sample annealed at 700 °C (Fig. 5f), reflections corresponding to Cu_2S (ICDD card no: 00-003-1071), CuS (ICDD card no: 01-078-2122) and SnS (ICDD card no: 00-022-0953), SnS_2 (00-031-1399), ZnS (ICDD card no: 01-089-2196) are also present along with the main phase (i.e. CZTS). In both cases (i.e. Fig. 5e, f), the occurrence of SnS and CuS is possibly due to
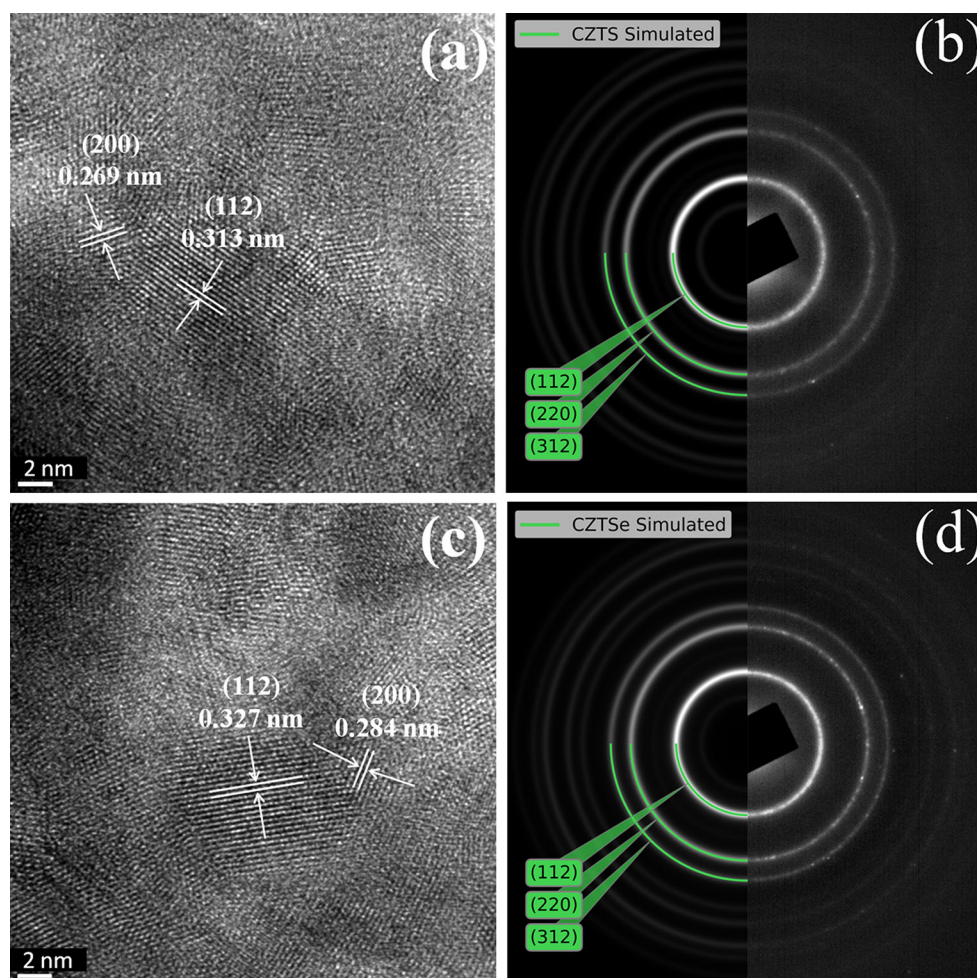
Fig. 4 HREM images show the fringes corresponding to (112) and (200) planes of CZTS (**a**) and CZTSe (**c**) respectively. SAED pattern of CZTS (**b**) and CZTSe (**d**) represents the ring profile, where the clearly visible rings correspond to the (112), (220) and (312) planes corroborating our XRD results shown in Fig. 1

degradation of the Cu_2S and SnS_2 due to evaporation of Sulfur at higher temperature (i.e. T > 500 °C).

In all the cases shown in Fig. 5a–f, the major peaks could correspond to the (112), (220) and (312) planes of CZTS, in the kesterite structure according to ICDD card nos: 026-0575 and 00-034-1246. The data in Fig. 5 are also in good agreement with literature reports on the CZTS [80–83]. Since the peaks of binary phases are evident in Fig. 5e, f, it can be confirmed that the samples annealed at 600 and 700 °C were not phase pure CZTS. Further, in such conditions, as per the reaction pathway (determined by the XRD and Raman spectra (Figs. 1a, 2a) discussed earlier, the presence of ZnS and Cu_2SnS_3 cannot be ruled out. Therefore, all the major peaks in Fig. 5e, f are also indexed to ZnS and Cu_2SnS_3.

Assuming that the quaternary kesterite phase has been synthesized, the lattice parameters for the CZTS sample (annealed at 500 °C) were determined to be a = b = 5.423 Å, c = 10.859 Å.

Figure 6 shows the XRD pattern of the as synthesized CZTSe sample as well as for the annealed at various temperatures. As already mentioned in earlier (Fig. 1b), the as-synthesized sample of CZTSe shown in Fig. 6a exhibits major peaks at $2\theta = 27.44°$, 45.44° and 53.67°, corresponding to d-spacings of 3.248, 1.994 and 1.706 Å.

XRD pattern corresponding to the CZTSe sample, annealed at 300 °C (Fig. 6b), exhibits major peaks at 2θ values of 27.30°, 45.27° and 53.54° corresponding to d-spacings of 3.263, 2.001 and 1.710 Å respectively. The sample corresponding to annealing at 400 °C (Fig. 6c) exhibits major peaks at $2\theta = 27.28°$, 45.14° and 53.52° corresponding to d-spacings of 3.265, 2.006 and 1.710 Å respectively. Similarly, the sample corresponding to 500 °C annealing temperature (Fig. 6d) exhibits peaks at $2\theta = 27.17°$, 45.11° and 53.44° corresponding to d-spacings of 3.278, 2.008 and 1.713 Å.

In case of samples annealed at 600 °C (Fig. 6e), in addition to the peaks corresponding to CZTSe, peaks of

Fig. 5 XRD patterns of CZTS sample prepared by 30 h wet ball milling (as synthesized as well as annealed at various temperatures)
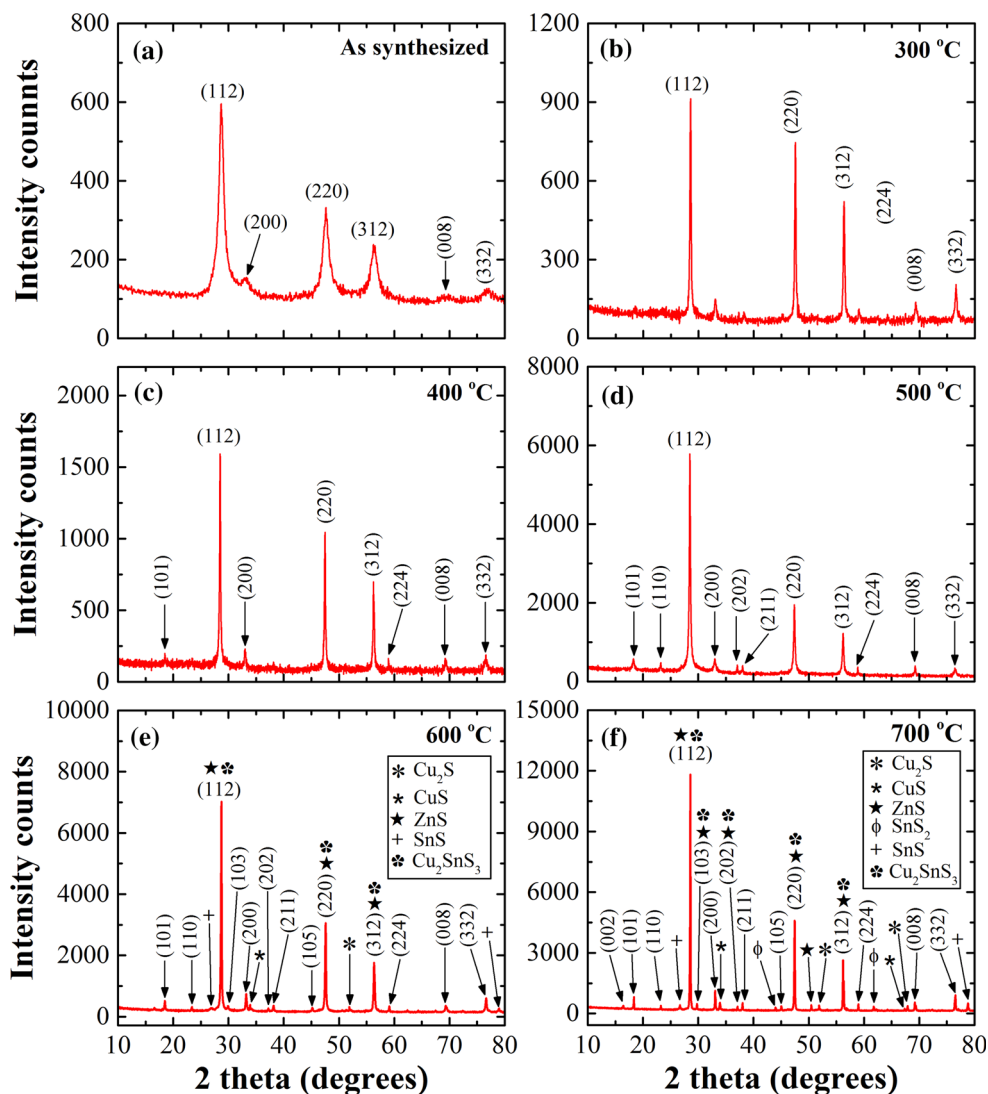
binary phases such as; Cu_2Se (ICDD card no: 00-027-1131), CuSe (ICDD card no: 00-049-1457) and $SnSe_2$ (ICDD card no: 00-023-0602) are also present. The reason of occurrence of binary phases at higher temperature ($T > 580$ °C) is well explained in literature [50]. Similarly, in case of sample annealed at 700 °C (Fig. 6f), reflections corresponding to Cu_2Se (ICDD card no: 00-027-1131), SnSe (ICDD card no: 00-032-1382), $SnSe_2$ (00-023-0602) are also present along with the main phase (i.e. CZTSe). The occurrence of SnSe and CuSe (Fig. 6e, f) is possibly due to degradation of the Cu_2Se and $SnSe_2$ due to evaporation of Selenium at higher temperature (i.e. $T > 500$ °C).

Analogous to the case of CZTS, in all the cases shown in Fig. 6a–f, the major peaks could correspond to the (112), (220) and (312) planes of CZTSe, in the kesterite structure according to ICDD card nos: 00-052-0868 and 01-080-6853. The data shown in Fig. 6 are also in good agreement with literature reports on the CZTSe [84, 85]. Since the

peaks of binary phases are evident in Fig. 6e, f, it can be confirmed that the samples annealed at 600 and 700 °C were not phase pure CZTSe. Further, in such conditions, as per the reaction pathway (determined by the XRD and Raman spectra (Figs. 1b, 2b) discussed earlier, the presence of ZnSe and Cu_2SnSe_3 cannot be ruled out. Therefore, all the major peaks in Fig. 6e, f are also indexed to ZnSe and Cu_2SnSe_3.

The FWHM of the various peaks corresponding to Figs. 5 and 6 was used to calculate the crystallite size using the Scherrer's equation [86], and the values obtained are summarized in Table 1. XRD data analyzed in Table 1 only represents the near phase pure samples (i.e. samples annealed up to 500 °C).

It can be inferred that the as-synthesized samples consisted of crystallites that have hardly been subject to grain growth; the subsequent lower temperature annealing step (300 °C) assisted in stress relief in the lattice and the

Fig. 6 XRD patterns of CZTSe sample prepared by 30 h wet ball milling (as synthesized as well as annealed at various temperatures)
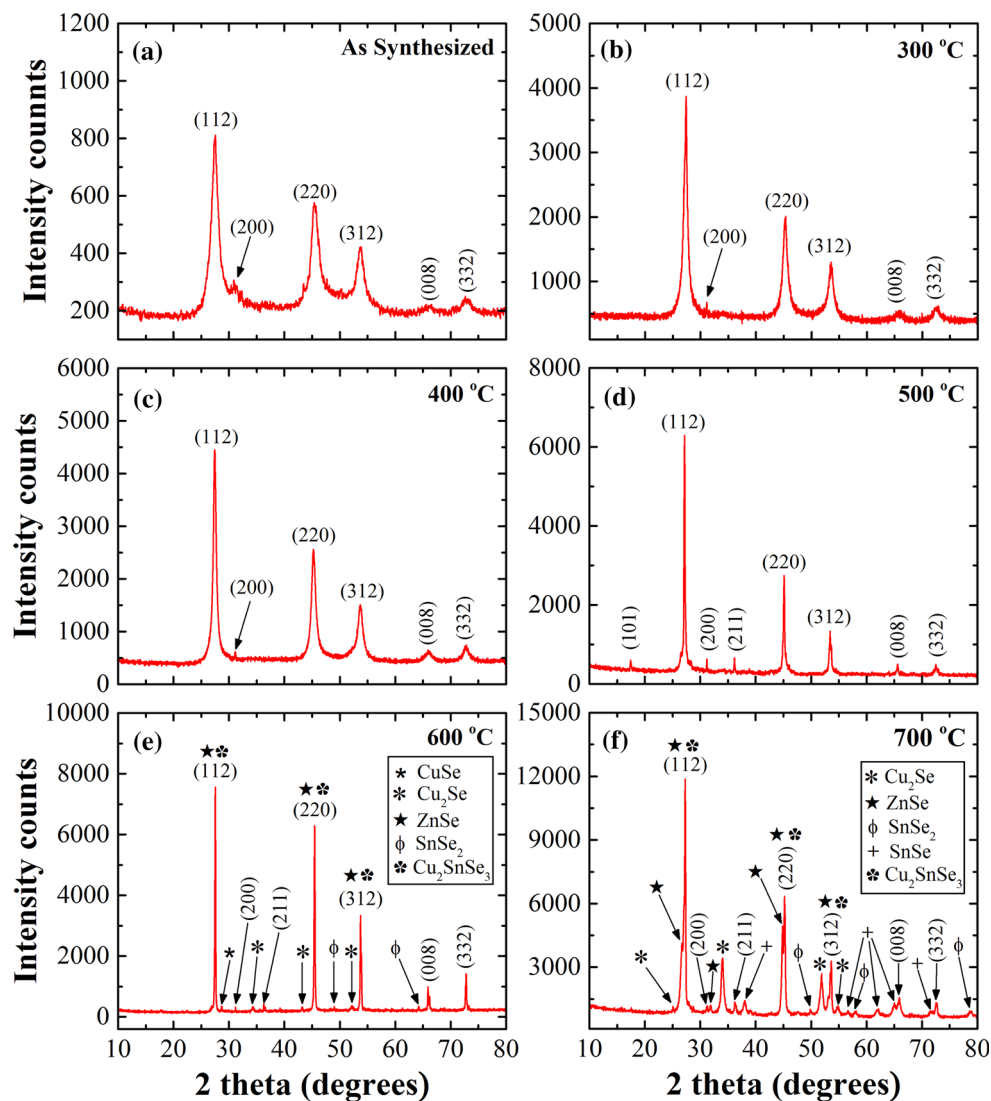
conversion of disordered kesterite to ordered kesterite. The same is evident from the higher 2θ shift in case of as synthesized to annealed sample (@ 300 °C) as compared to that in case of 300–400 and 400–500 °C. With more energy (i.e. higher temperature), first the stress relief and conversion of disordered kesterite to ordered kesterite takes places and thereafter the grain grown takes place. The detail discussion on the XRD and Raman peak shifting after annealing can be found elsewhere [50, 87, 88].

To determine the band gap of CZTS/Se samples, as synthesized nano crystalline CZTS and CZTSe powders were spin coated on a glass substrate to form a film of thickness ≈2 μm. Optical transmission (T) and reflection (R) measurements for as synthesized as well as annealed films of CZTS and CZTSe were taken at room temperature. The optical absorption coefficient (α) was determined using the formula [89, 90]:

$$\alpha = \frac{1}{t} ln \left[\frac{(1-R)^2}{T} \right]$$

where t is the thickness of the film. The optical band gap of the samples were obtained by extrapolating the linear region of the plot $(\alpha h\nu)^2$ versus photon energy ($h\nu$).

Figure 7a, b shows the absorption coefficient (α) *v/s* wavelength (λ) *plot* for as synthesized phase pure CZTS and CZTSe respectively. Both the CZTS as well as CZTSe samples exhibited high optical absorption from visible to near IR region, which is in consistant with the literature [91]. It can be seen that for both CZTS as well as CZTSe, the absorption coefficient is in the order of $\sim 10^4$/cm in the visible region, which is suitable for thin film PV applications. Since the thin films are as such not the sintered reflecting films, these were the spread nano-particles. Therefore, the reflectance was found negligible in all the

Table 1 Calculated crystallite size of the as-synthesized and annealed CZTS and CZTSe samples

(hkl)	2θ (°)	FWHM (°)	D (nm)
CZTS			
As Synthesized			
(112)	28.71	0.8309	9.76
(220)	47.61	1.0081	8.52
(312)	56.35	1.0448	8.53
Annealed (300 °C)			
(112)	28.56	0.2796	29.01
(220)	47.53	0.2840	30.24
(312)	56.33	0.3162	28.19
Annealed (400 °C)			
(112)	28.51	0.2596	31.24
(220)	47.46	0.2676	32.08
(312)	56.26	0.3011	29.60
Annealed (500 °C)			
(112)	28.49	0.1840	44.07
(220)	47.39	0.3289	26.10
(312)	56.22	0.2448	36.40
CZTSe			
As Synthesized			
(112)	27.44	1.0597	7.63
(220)	45.44	0.9750	8.74
(312)	53.67	1.0488	8.40
Annealed (300 °C)			
(112)	27.30	0.8008	10.10
(220)	45.27	0.9655	8.82
(312)	53.54	1.0160	8.66
Annealed (400 °C)			
(112)	27.28	0.4842	16.70
(220)	45.14	0.4080	20.86
(312)	53.52	0.6528	13.48
Annealed (500 °C)			
(112)	27.17	0.1415	57.14
(220)	45.11	0.1800	47.28
(312)	53.44	0.2190	40.18

D denotes the calculated crystallite size for each sample

cases. Tauc plot shown in inset of Fig. 7 was used to calculate the band gap of CZTS (a) and CZTSe (b) sample.

Table 2 shows the SEM–EDS analysis and band gap of the CZTS as well as CZTSe samples annealed at various temperatures (i.e. 300–700 °C). It can be seen that; up to annealing temperature of 500 °C, the samples are very close to the Cu_2ZnSnX_4 (X: S, Se) stoichiometry, since the deviation in the stoichiometry of the samples are within the measurement accuracy of the SEM–EDS instrument.
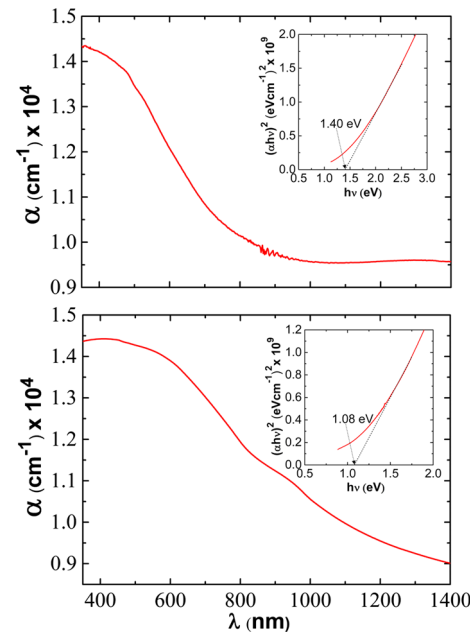
Fig. 7 Absorption coefficient v/s wavelength curve (*inset* obtained band gap) for as synthesized CZTS (**a**) and CZTSe (**b**) samples

It can be seen that the band gap of CZTS as well as CZTSe is increasing with annealing temperature up to 500 °C. The possible reason behind this is, co-existence of various crystal structures such as kesterite, stannite and PMCA (primitive mixed Cu–Au like structure) in the as synthesized samples, as discussed in literature [92–94]. For the sample annealed at T ≥ 600 °C, the composition of both CZTS as well as CZTSe becomes slightly Sn and S/Se poor. Under Sn deficiency, due to their lowest formation energy, acceptor defects such as; Cu_{Sn} and Zn_{Sn} are probable candidates [95]. Due to slightly Cu rich conditions, the most possible defect could be Cu_{Sn}, which has the ionization energy around 0.28 eV [96]. Therefore the reduction in the observed band gap of CZTS as well as CZTSe samples after annealing at T ≥ 600 °C are possibly due to presence of Cu_{Sn} defect. Similar findings for Sn poor composition for CZTS have been discussed in detail elsewhere [97]. Further under Cu rich conditions analogous to present case, a reported PL study also confirms such observations [96]. The observed values of the band gaps for both CZTS as well as CZTSe are in good agreement with those reported in the literature [12, 51, 98–104]. Above discussion suggests the suitable annealing temperature for CZTS as well as CZTSe should be T ≤ 500 °C. For all the samples of CZTS/Se, the absorption coefficient α was found to be of the order of 10^4 cm^{-1} in the visible region of the solar spectrum which suggests their utility as a light absorber material in solar PV applications.

Table 2 Effect of annealing temperature on composition and band gap of CZTS and CZTSe

Annealing temperature	Atomic percentage (%)				Band gap (eV)
	Cu	Zn	Sn	S	
CZTS					
300 °C	25.17	12.23	11.58	51.02	1.51
400 °C	25.29	12.56	11.41	50.74	1.53
500 °C	26.44	12.77	11.33	49.46	1.60
600 °C	28.36	13.11	10.72	47.81	1.46
700 °C	29.89	13.77	9.43	46.91	1.42
As synthesized	24.66	12.46	11.60	51.28	1.40

Annealing temperature	Atomic percentage (%)				Band gap (eV)
	Cu	Zn	Sn	Se	
CZTSe					
300 °C	25.21	13.04	11.71	50.04	1.10
400 °C	25.57	13.11	11.52	49.80	1.10
500 °C	26.61	13.15	11.28	48.96	1.18
600 °C	27.25	13.67	10.97	48.11	1.12
700 °C	28.89	13.82	9.91	47.38	1.09
As synthesized	24.73	12.72	11.92	50.63	1.08

4 Conclusion

The reaction pathway for CZTS/Se formation using mechano-chemical synthesis via ballmilling of elemental precursors has been determined experimentally. Series of ballmilling experiments of 5–30 h duration and the sample analysis using XRD and Raman tools has provided the information on presence of binary and ternary phases in samples prepared during each experiment. The phase tracking in various experiments of 5–30 h duration suggests the formation of binary sulphides/selenides at first place and thereafter formation of ternary phase $Cu_2Sn(S/Se)_3$ and ZnS/Se. The presence of binary phases for longer duration in case of CZTSe as compared to CZTS is supported by the comparison of formation enthalpies of Cu_2SnSe_3 and Cu_2SnS_3. The final reaction of ternary phase and ZnS/Se yields quaternary phase CZTS/Se. A very useful finding of the reaction pathway is that the use of binary sulphide/selenide will not help in reducing the reaction duration due to the fact that the formation of binaries takes least amount of time (i.e. less than 5 h ballmilling duration). The time consuming or more energy intensive part of the entire reaction sequence is the conversion from binaries to quaternary phase. The proposed process and obtained reaction pathway can be useful in obtaining CZTS/Se materials in single phase for bulk production using scalable ballmilling technique. Further the crystallite growth from 9.76 to ~44 and 7.63 to ~57 nm has been achieved by

annealing of the samples. For phase confirmation, the synthesized materials were well characterized using the different characterization tools like XRD, Raman spectroscopy, XPS, SEM–EDS, TEM and UV–Vis. XRD and Raman revealed the formation of phase pure kesterite for both CZTS and CZTSe, absence of any secondary phase is evident from these studies as well as by XPS. The simulated ring patterns obtained using the diffraction ring profiler were found to be in good agreement to the ring patterns obtained using TEM-SAED for the different planes [(112), (220) and (312)] of CZTS/Se. On annealing, it has been observed that the T ≤ 500 °C was the suitable condition for both the CZTS and CZTSe for appropriate grain growth. At higher temperature (i.e. T ≥ 600 °C), both the compounds (CZTS and CZTSe) starts to deteriorate and forms secondary phases. The band gap for CTZS was observed to be in the range of 1.40–1.60 eV and that of CZTSe was in the range of 1.08–1.18 eV. The high absorption coefficient of CZTS as well as CZTSe, i.e. $\sim 10^4$ cm^{-1} suggests their suitability as absorber materials in thin film based solar photovoltaics.

References

1. K. Ito, T. Nakazawa, Jpn. J. Appl. Phys. **27**, 2094 (1988)
2. J. Seol, S. Lee, J. Lee, H. Nam, K. Kim, Sol. Energy Mater. Sol. Cells **75**, 155 (2003)
3. J. Zhang, L. Shao, Y. Fu, E. Xie, Rare Met. **25**, 315 (2006)
4. K. Jimbo, R. Kimura, T. Kamimura, S. Yamada, W.S. Maw, H. Araki, K. Oishi, H. Katagiri, Thin Solid Films **515**, 5997 (2007)
5. H. Katagiri, K. Jimbo, S. Yamada, T. Kamimura, W.S. Maw, T. Fukano, T. Ito, T. Motohiro, Appl. Phys. Express **1**, 041201 (2008)
6. N. Momose, M.T. Htay, T. Yudasaka, S. Igarashi, T. Seki, S. Iwano, Y. Hashimoto, K. Ito, Jpn. J. Appl. Phys. **50**, 01BG091 (2011)
7. C. Platzer-Björkman, J. Scragg, H. Flammersberger, T. Kubart, M. Edoff, Sol. Energy Mater. Sol. Cells **98**, 110 (2011)
8. M. Kemell, M. Ritala, M. Leskelä, Crit. Rev. Solid State Mater. Sci. **30**, 1 (2005)
9. T.M. Friedlmeier, N. Wieser, T. Walter, H. Dittrich, H.-W. Schock, in *Proceedings of 14th European Photovoltaic Solar Energy Conference* (1997), pp. 1242–1245
10. H. Katagiri, N. Sasaguchi, S. Hando, S. Hoshino, J. Ohashi, T. Yokota, Sol. Energy Mater. Sol. Cells **49**, 407 (1997)
11. H. Katagiri, K. Saitoh, T. Washio, H. Shinohara, T. Kurumadani, S. Miyajima, Sol. Energy Mater. Sol. Cells **65**, 141 (2001)
12. H. Katagiri, N. Ishigaki, K. Hironori, I. Naoya, I. Takeshi, Jpn. J. Appl. Phys. **40**, 500 (2001)
13. T. M. Friedlmeier, H. Dittrich, and H.W. Schock, in *11th Conference Ternary Multinary Compounds ICTMC-11, Salford*, 8–12 September 1997 (1998), pp. 345–348
14. S. Ahn, S. Jung, J. Gwak, A. Cho, K. Shin, K. Yoon, D. Park, H. Cheong, J.H. Yun, Appl. Phys. Lett. **97**, 021905 (2010)
15. T. Tanaka, D. Kawasaki, M. Nishio, Q. Guo, H. Ogawa, Phys. Status Solidi **3**, 2844 (2006)
16. A. Weber, H. Krauth, S. Perlt, B. Schubert, I. Kötschau, S. Schorr, H.W. Schock, Thin Solid Films **517**, 2524 (2009)
17. B. Schubert, B. Marsen, S. Cinque, T. Unold, R. Klenk, S. Schorr, H. Schock, Prog. Photovolt. Res. Appl. **19**, 93 (2011)
18. T. Tanaka, A. Yoshida, D. Saiki, K. Saito, Q. Guo, M. Nishio, T. Yamaguchi, Thin Solid Films **518**, S29 (2010)
19. K. Wang, O. Gunawan, T. Todorov, B. Shin, S.J. Chey, N.A. Bojarczuk, D. Mitzi, S. Guha, Appl. Phys. Lett. **97**, 143508 (2010)
20. B. Shin, O. Gunawan, Y. Zhu, N.A. Bojarczuk, S.J. Chey, S. Guha, Prog. Photovolt. Res. Appl. **21**, 72 (2013)
21. K. Sekiguchi, K. Tanaka, K. Moriya, H. Uchiki, Phys. Status Solidi **3**, 2618 (2006)
22. S.M. Pawar, A.V. Moholkar, I.K. Kim, S.W. Shin, J.H. Moon, J.I. Rhee, J.H. Kim, Curr. Appl. Phys. **10**, 565 (2010)
23. L. Sun, J. He, Y. Chen, F. Yue, P. Yang, J. Chu, J. Cryst. Growth **361**, 147 (2012)
24. A.V. Moholkar, S.S. Shinde, A.R. Babar, K.-U. Sim, Y. Kwon, K.Y. Rajpure, P.S. Patil, C.H. Bhosale, J.H. Kim, Sol. Energy **85**, 1354 (2011)
25. A.V. Moholkar, S.S. Shinde, G.L. Agawane, S.H. Jo, K.Y. Rajpure, P.S. Patil, C.H. Bhosale, J.H. Kim, J. Alloys Compd. **544**, 145 (2012)
26. G.D. Surgina, A.V. Zenkevich, I.P. Sipaylo, V.N. Nevolin, W. Drube, P.E. Teterin, M.N. Minnekaev, Thin Solid Films **535**, 44 (2013)
27. S. Taunier, J. Sicx-Kurdi, P.P. Grand, A. Chomont, O. Ramdani, L. Parissi, P. Panheleux, N. Naghavi, C. Hubert, M. Ben-Farah, J.P. Fauvarque, J. Connolly, O. Roussel, P. Mogensen, E. Mahé, J.F. Guillemoles, D. Lincot, O. Kerrec, Thin Solid Films **480–481**, 526 (2005)
28. D.R. Johnson, Thin Solid Films **361–362**, 321 (2000)
29. J.J. Scragg, P.J. Dale, L.M. Peter, Electrochem. Commun. **10**, 639 (2008)
30. J.J. Scragg, P.J. Dale, L.M. Peter, Thin Solid Films **517**, 2481 (2009)
31. J.J. Scragg, D.M. Berg, P.J. Dale, J. Electroanal. Chem. **646**, 52 (2010)
32. J.J. Scragg, P.J. Dale, L.M. Peter, G. Zoppi, I. Forbes, Phys. Status Solidi **245**, 1772 (2008)
33. A. Ennaoui, M. Lux-Steiner, A. Weber, D. Abou-Ras, I. Köt-schau, H.W. Schock, R. Schurr, A. Hölzing, S. Jost, R. Hock, T. Voß, J. Schulze, A. Kirbs, Thin Solid Films **517**, 2511 (2009)
34. X. Zhang, X. Shi, W. Ye, C. Ma, C. Wang, Appl. Phys. A Mater. Sci. Process. **94**, 381 (2009)
35. S. Ahmed, K.B.K. Reuter, O. Gunawan, L. Guo, L.T. Roman-kiw, H. Deligianni, Adv. Energy Mater. **2**, 253 (2012)
36. K. Tanaka, N. Moritake, H. Uchiki, Sol. Energy Mater. Sol. Cells **91**, 1199 (2007)
37. K. Tanaka, M. Oonuki, N. Moritake, H. Uchiki, Sol. Energy Mater. Sol. Cells **93**, 583 (2009)
38. N. Moritake, Y. Fukui, M. Oonuki, K. Tanaka, H. Uchiki, Phys. Status Solidi **6**, 1233 (2009)
39. T. Todorov, M. Kita, J. Carda, P. Escribano, Thin Solid Films **517**, 2541 (2009)
40. C. Steinhagen, M.G. Panthani, V. Akhavan, B. Goodfellow, B. Koo, B.A. Korgel, J. Am. Chem. Soc. **131**, 12554 (2009)
41. P. Dai, X. Shen, Z. Lin, Z. Feng, H. Xu, J. Zhan, Chem. Commun. (Camb.) **46**, 5749 (2010)
42. Y. Wang, H. Gong, J. Alloys Compd. **509**, 9627 (2011)
43. Z. Zhou, Y. Wang, D. Xu, Y. Zhang, Sol. Energy Mater. Sol. Cells **94**, 2042 (2010)
44. R. Saravana Kumar, B.D. Ryu, S. Chandramohan, J.K. Seol, S.-K. Lee, C.-H. Hong, Mater. Lett. **86**, 174 (2012)
45. N. Nakayama, K. Ito, Appl. Surf. Sci. **92**, 171 (1996)
46. N. Kamoun, H. Bouzouita, B. Rezig, Thin Solid Films **515**, 5949 (2007)
47. Y.B. Kishore Kumar, G. Suresh Babu, P. Uday Bhaskar, V. Sundara Raja, Sol. Energy Mater. Sol. Cells **93**, 1230 (2009)
48. Y.B. Kishore Kumar, G. Suresh Babu, P. Uday Bhaskar, V. Sundara Raja, Phys. Status Solidi **206**, 1525 (2009)
49. T. Prabhakar, J. Nagaraju, in *35th IEEE Photovoltaic Specialists Conference* (2010), pp. 1964–1969
50. D. Pareek, K.R. Balasubramaniam, P. Sharma, Mater. Charact. **103**, 42 (2015)
51. Q.M. Chen, Z.Q. Li, Y. Ni, S.Y. Cheng, X.M. Dou, Chin. Phys. B **21**, 038401 (2012)
52. Q.M. Chen, X.M. Dou, Z.Q. Li, S.Y. Cheng, S.L. Zhuang, Adv. Mater. Res. **335–336**, 1406 (2011)
53. B. Pani, U.P. Singh, J. Renew. Sustain. Energy **5**, 0531311 (2013)
54. G. Brammertz, M. Buffière, S. Oueslati, H. Elanzeery, K. Ben Messaoud, S. Sahayaraj, C. Köble, M. Meuris, J. Poortmans, Appl. Phys. Lett. **103**, 163904 (2013)
55. T.K. Todorov, K.B. Reuter, D.B. Mitzi, Adv. Mater. **22**, E156 (2010)
56. D.A.R. Barkhouse, O. Gunawan, T. Gokmen, T.K. Todorov, D.B. Mitzi, Prog. Photovolt. Res. Appl. **20**, 6 (2012)
57. T.K. Todorov, J. Tang, S. Bag, O. Gunawan, T. Gokmen, Y. Zhu, D.B. Mitzi, Adv. Energy Mater. **3**, 34 (2013)
58. W. Wang, M.T. Winkler, O. Gunawan, T. Gokmen, T.K. Todorov, Y. Zhu, D.B. Mitzi, Adv. Energy Mater. **4**, 1301465 (2014)
59. A. Polman, M. Knight, E.C. Garnett, B. Ehrler, W.C. Sinke, Science **352**, aad4424 (2016)

60. S. Schorr, A. Weber, V. Honkimäki, H.W. Schock, Thin Solid Films **517**, 2461 (2009)
61. I.D. Olekseyuk, I.V. Dudchak, L.V. Piskach, J. Alloys Compd. **368**, 135 (2004)
62. A. Weber, R. Mainz, H.W. Schock, J. Appl. Phys. **107**, 013516 (2010)
63. L. Takacs, Prog. Mater Sci. **47**, 355 (2002)
64. C.P. Liu, C.L. Chuang, Powder Technol. **229**, 78 (2012)
65. L. Zaluski, A. Zaluska, J. Ström-Olsen, J. Alloys Compd. **290**, 71 (1999)
66. H.C. Kang, D.K. Jun, B. Jin, E.M. Jin, K.H. Park, H.B. Gu, K.W. Kim, J. Power Sources **179**, 340 (2008)
67. T.S. Shyju, S. Anandhi, R. Suriakarthick, R. Gopalakrishnan, P. Kuppusami, J. Solid State Chem. **227**, 165 (2015)
68. C.E.M. Campos, K. Ersching, J.C. de Lima, T.A. Grandi, H. Höhn, P.S. Pizani, J. Alloys Compd. **466**, 80 (2008)
69. D. Pareek, K.R. Balasubramaniam, P. Sharma, RSC Adv. **6**, 68754 (2016)
70. S. Mehdaoui, N. Benslim, O. Aissaoui, M. Benabdeslem, L. Bechiri, A. Otmani, X. Portier, G. Nouet, Mater. Charact. **60**, 451 (2009)
71. C. Dun, N.A.W. Holzwarth, Y. Li, W. Huang, D.L. Carroll, J. Appl. Phys. **115**, 1935131 (2014)
72. S.V. Baryshev, E. Thimsen, Chem. Mater. **27**, 2294 (2015)
73. X. Fontane, V. Izquierdo-Roca, A. Fairbrother, M. Espindola-Rodriguez, S. Lopez-Marino, M. Placidi, T. Jawhari, E. Saucedo, A. Perez-Rodriguez, in *2013 IEEE 39th Photovoltaic Specialists Conference* (IEEE), (2013), pp. 2581–2584
74. S.C. Riha, B.A. Parkinson, A.L. Prieto, J. Am. Chem. Soc. **131**, 12054 (2009)
75. C. Calderón, G. Gordillo, R. Becerra, P. Bartolo-Pérez, Mater. Sci. Semicond. Process. **39**, 492 (2015)
76. J. Xu, X. Yang, Q.-D. Yang, T.-L. Wong, C.-S. Lee, J. Phys. Chem. C **116**, 19718 (2012)
77. G. Gordillo, C. Calderon, P. Bartolo-Perez, Appl. Surf. Sci. **305**, 506 (2014)
78. S. Das, K.C. Mandal, Jpn. J. Appl. Phys. **52**, 125502 (2013). doi:10.7567/JJAP.52.125502
79. L. Zhang, C.M.B. Holt, E.J. Luber, B.C. Olsen, H. Wang, M. Danaie, X. Cui, X. Tan, V.W. Lui, W.P. Kalisvaart, D. Mitlin, J. Phys. Chem. C **115**, 24381 (2011)
80. Y. Xia, Z. Chen, Z. Zhang, X. Fang, G. Liang, Nanoscale Res. Lett. **9**, 208 (2014)
81. X. Zhai, H. Jia, Y. Zhang, Y. Lei, J. Wei, Y. Gao, J. Chu, W. He, J. Yin, Z. Zheng, CrystEngComm **16**, 6244 (2014)
82. K.U. Isah, J.A. Yabagi, U. Ahmadu, M. Isah, M. Gaetan, Z. Kana, A.A. Oberafo, ISOR J. Appl. Phys. **2**, 14 (2013)
83. W. Xie, X. Jiang, C. Zou, D. Li, J. Zhang, J. Quan, L. Shao, Phys. E Low Dimens. Syst. Nanostruct. **45**, 16 (2012)
84. K. Liu, N. Ji, L. Shi, H. Liu, J. Nanomater. **2014**, 1 (2014)
85. T. Rath, W. Haas, A. Pein, R. Saf, E. Maier, B. Kunert, F. Hofer, R. Resel, G. Trimmel, Sol. Energy Mater. Sol. Cells **101**, 87 (2012)
86. P. Scherrer, G. Nachrichten, Math. Phys. **2**, 98 (1918)
87. V. Kheraj, K.K. Patel, S.J. Patel, D.V. Shah, J. Cryst. Growth **362**, 174 (2013)
88. M.D. Regulacio, C. Ye, S.H. Lim, M. Bosman, E. Ye, S. Chen, Q.-H. Xu, M.-Y. Han, Chem. A Eur. J. **18**, 3127 (2012)
89. X. Lin, J. Kavalakkatt, K. Kornhuber, S. Levcenko, M.C. Lux-Steiner, A. Ennaoui, Thin Solid Films **535**, 10 (2013)
90. J.I. Pankove, *Optical Processes in Semiconductors* (Devor Publications, New York, 1975)
91. J. Wang, X. Xin, Z. Lin, Nanoscale **3**, 3040 (2011)
92. S. Chen, X.G. Gong, A. Walsh, S.-H. Wei, Appl. Phys. Lett. **94**, 041903 (2009)
93. S. Schorr, H.J. Hoebler, M. Tovar, Eur. J. Mineral. **19**, 65 (2007)
94. S. Schorr, Thin Solid Films **515**, 5985 (2007)
95. S. Chen, J.H. Yang, X.G. Gong, A. Walsh, S.-H. Wei, Phys. Rev. B **81**, 245204 (2010)
96. M. Grossberg, J. Krustok, J. Raudoja, T. Raadik, Appl. Phys. Lett. **101**, 102102 (2012)
97. C. Malerba, F. Biccari, C. Leonor, A. Ricardo, J. Alloys Compd. **582**, 528 (2014)
98. C.P. Chan, Z. Chen, H. Lam, C. Surya, in *Proceedings of SPIE* (2009), pp. 7411081–7411089
99. F. Biccari, R. Chierchia, M. Valentini, P. Mangiapane, E. Salza, C. Malerba, C.L.A. Ricardo, L. Mannarino, P. Scardi, A. Mittiga, Energy Procedia **10**, 187 (2011)
100. Y. Li, Q. Han, T.W. Kim, W. Shi, Nanoscale **6**, 3777 (2014)
101. B.D. Chernomordik, A.E. Béland, N.D. Trejo, A.A. Gunawan, D.D. Deng, K.A. Mkhoyan, E.S. Aydil, J. Mater. Chem. A **2**, 10389 (2014)
102. M.I. Amal, S.H. Lee, K.H. Kim, Curr. Appl. Phys. **14**, 916 (2014)
103. K. Woo, Y. Kim, W. Yang, K. Kim, I. Kim, Y. Oh, J.Y. Kim, J. Moon, Sci. Rep. **3**, 3069 (2013)
104. C. Shi, G. Shi, Z. Chen, P. Yang, M. Yao, Mater. Lett. **73**, 89 (2012)